Asian Journal of Chemistry; Vol. 38, No. 5 (2026), 1295-1307
ASIAN JOURNAL OF CHEMISTRY
https://doi.org/10.14233/ajchem.2026.35660

Effect of Ni Substitution on the Structural and Electrochemical Properties of $ZnFe_2O_4$ for Supercapacitor Applications

S. ANBUKARUPPUCHAMY[1,*], P. BALAMURUGAN[1], P. VIJAYAMATHUBALAN[1], JANET DAYANITHI[2] and J. VIDYA[3]

[1]Department of Physics, Government Arts College, Nandanam, Chennai-600035, India
[2]Department of Chemistry, School of Basic Science, VISTAS, Pallavaram, Chennai-600117, India
[3]Department of Physics, Arignar Anna Government Arts College, Namakkal-637002, India

*Corresponding author: E-mail: loveaksamy@gmail.com

Received: 27 January 2026 *Accepted*: 6 April 2026 *Published online*: 4 May 2026 AJC-22355

$Ni_xZn_{1-x}Fe_2O_4$ (x = 0, 0.3, 0.5) nanoparticles were synthesised *via* a sol-gel auto-combustion method to examine the effect of Ni substitution on $ZnFe_2O_4$, with emphasis on their structural, optical, morphological, compositional, oxidation state and electrochemical properties. PXRD analysis confirmed the formation of a single-phase cubic spinel structure with crystallite size from 39.74 to 36.06 nm, while UV-Vis analysis showed that the bandgap energy gradually decreases with increasing nickel concentration. FTIR and Raman spectra validated the characteristic M–O vibrational modes of the spinel structure. FESEM studies revealed particle-like morphologies with moderate clusters, and a decrease in average NP size from 48 nm to 41 nm as the Ni content increased. EDX and XPS analyses verified the elemental composition and oxidation states without the presence of impurity phases. Electrochemical studies demonstrated pronounced pseudocapacitive behaviour, with the $Ni_{0.5}Zn_{0.5}Fe_2O_4$ electrode delivering a maximum specific capacitance of 250 F g^{-1} at 1 A g^{-1}. Furthermore, it exhibited an energy density of 22.31 Wh kg^{-1} and a power density of 400 W kg^{-1}, along with reasonable cycling stability, retaining 91.54% of its initial capacitance after 200 cycles. Electrochemical impedance spectroscopy indicated reduced charge-transfer resistance and improved ion diffusion kinetics upon Ni substitution. Among all compositions, the x = 0.5 sample demonstrated the most balanced electrochemical performance, highlighting its potential as an efficient electrode material for high-performance supercapacitor applications.

Keywords: Electrochemical energy storage, Supercapacitors, Pseudocapacitors, Spinel ferrites, Molecular-level modification.

INTRODUCTION

With increasing global energy demand and the environmental impact of fossil fuels, the development of efficient energy storage systems has become essential. Among electrochemical storage devices, supercapacitors have gained significant attention due to their high power density, rapid charge–discharge capability, long cycle life and environmental compatibility. Their performance is governed by electrochemical processes at the electrode–electrolyte interface involving either electrostatic charge storage in electric double-layer capacitors (EDLCs) or fast faradaic reactions in pseudocapacitors [1-6].

In both classes of supercapacitors, electrochemical performance is governed by critical parameters, including surface area, pore distribution and material conductivity [7]. Nowadays, pseudocapacitors utilize various transition metal oxides (TMOs) and conducting polymers for electrode fabrication due to their ability to provide high specific capacitance and energy density [8]. Among the transition metal oxides, the spinel structure (AB_2O_4) is well known for its high stability and adaptability due to its unique cation arrangement. Specifically, spinel ferrites (MFe_2O_4, M = Mn, Zn, Co, Ni, *etc.*) exhibit rich redox chemistry because of their multiple accessible oxidation states; their high ionic conductivity and robust structure make them suitable for supercapacitor applications [9-12]. For instance, Aparna *et al.* [9] demonstrated that the capacitance of $ZnFe_2O_4$ and $MnFe_2O_4$ electrodes which shows 138 F g^{-1} and 190 F g^{-1} respectively, at 2 mV s^{-1}, while $ZnFe_2O_4$ exhibit 90% retention after 1000 cycles. Kotutha *et al.* [13] revealed that $CoFe_2O_4$ electrode exhibits 65.5 F g^{-1} specific capacitance at 10 mV s^{-1} and 90.9% retention after 1000 cycles. Whereas Lv *et al.* [14] reported the $CoFe_2O_4$ electrode, which delivered a specific capacitance of 142 F g^{-1} at s scan rate 2 mV s^{-1} and maintained 71.8% of its initial capacitance

This is an open access journal, and articles are distributed under the terms of the Attribution 4.0 International (CC BY 4.0) License. This license lets others distribute, remix, tweak, and build upon your work, even commercially, as long as they credit the author for the original creation. You must give appropriate credit, provide a link to the license, and indicate if changes were made.

after 1000 cycles. Cai *et al.* [15] demonstrated that $NiFe_2O_4$ electrode achieved a capacitance of 50 F g^{-1} at a current density 0.5 A g^{-1} with a retention 78.6% after 2000 charge discharge cycles. Among various spinel ferrites, pure zinc ferrite ($ZnFe_2O_4$) stands out due to its excellent structural stability, low cost and non-toxic nature [16]. Zhu *et al.* [17] reported that $ZnFe_2O_4$ microspheres 131 F g^{-1} at a current density 1 A g^{-1}, with 92% after 1000 cycles. However, its electrochemical performance is limited as it exhibits low electrical conductivity and sluggish charge transfer kinetics [17,18]. These studies highlight the need for molecular-level modification to improve the electrochemical performance of ferrite materials. For example, as reported by He *et al.* [19], the rGO-$CoFe_2O_4$ electrode showed a specific capacitance of 123.2 F cm^{-2} at 5 mA cm^{-2}, while retaining 78.1% of its capacitance after 1000 cycles. Kotutha *et al.* [13] reported that rGO–$CoFe_2O_4$ delivered a capacitance of 112.9 F g^{-1} at 10 mV s^{-1}, with 91.3% retention after 1000 cycles. Bhujun *et al.* [20] demonstrated that $CuCoFe_2O_4$ delivered a capacitance of 221 F g^{-1} at 5 mV s^{-1}, with an energy density of 7.90 Wh kg^{-1} and 80% retention after 200 cycles. Cai *et al.* [15] reported that rGO/$NiFe_2O_4$ achieved a capacitance of 215.7 F g^{-1} at 0.5 A g^{-1}, maintaining 89.4% retention after 2000 cycles. Li *et al.* [21] reported a specific capacitance of 94 F g^{-1} at a current density of 0.5 A g^{-1} for pure $ZnFe_2O_4$ nanoparticles.

On the other hand, the incorporation of nitrogen-reduced graphene (NRG) significantly improved the performance, yielding 244 F g^{-1} under identical conditions. Palanivel *et al.* [22] reported that $ZnFe_2O_4$/*g*-C_3N_4 delivered a capacitance of 103 F g^{-1} at 10 A g^{-1}, with 94% retention after 500 cycles. Saraf *et al.* [23] demonstrated that $ZnFe_2O_4$/GCE exhibited a capacitance of 175 F g^{-1} at 5 A g^{-1}, with 82.75% retention after 1000 cycles. Similarly, Sathiyamurthy *et al.* [24] demonstrated that pristine $ZnFe_2O_4$ electrodes delivered 146 F g^{-1} at a scan rate of 10 mV s^{-1}, while cobalt-substituted $ZnFe_2O_4$ ($Co_{0.5}Zn_{0.5}Fe_2O_4$) exhibited a markedly enhanced capacitance of 218 F g^{-1} at the same scan rate. Lin *et al.* [25] reported that $Co_{0.5}Ni_{0.5}Fe_2O_4$ achieved a capacitance of 113 F g^{-1} at 5 mV s^{-1}, with 120% retention after 1000 cycles. Costa *et al.* [26] reported that $Ni_{0.6}Zn_{0.4}Fe_2O_4$ and $Ni_{0.8}Zn_{0.2}Fe_2O_4$ exhibited a capacitance of 186.61 F g^{-1} and 136.55 F g^{-1}, respectively, at 1 A g^{-1}, with an energy density of 5.24 Wh kg^{-1} and 3.84 Wh kg^{-1}, respectively. These results demonstrate that controlled incorporation of transition metals into spinel $ZnFe_2O_4$ enhances conductivity and active site density, thereby improving the electrochemical performances [27,28].

In this study, the effects of Ni doping on the structural, optical, functional, morphological, elemental and electrochemical properties of $ZnFe_2O_4$ were systematically investigated using advanced characterisation techniques to assess its potential for supercapacitor applications.

EXPERIMENTAL

The chemicals, *viz.* $Ni(NO_3)_2{\cdot}6H_2O$, $Zn(NO_3)_2{\cdot}6H_2O$, $Fe(NO_3)_3{\cdot}9H_2O$ and citric acid ($C_6H_8O_7$, Sigma-Aldrich) were used as precursors without further purification. Electrode materials, including Ni foil, Na_2SO_4, polyvinylidene fluoride (PVDF) and N-methyl-2-pyrrolidinone (NMP) (SRL Chemicals), were used as received. Deionised water was used to clean the components and synthesis process.

Synthesis of spinel ferrites: $Ni_xZn_{1-x}Fe_2O_4$ (x = 0, 0.3, 0.5) nanoparticles were synthesised *via* a sol-gel auto combustion method. Initially, all nitrates and citric acid were dissolved separately in deionised water, then mixed together with constant stirring. Ammonia solution was added dropwise to adjust the pH to 7, resulting in the formation of brown sol. The mixture was heated to 100 ºC under continuous stirring until gel formation, after which self-ignition occurred, producing a fluffy, ash-like powder. This powder was heated at 180 ºC for 5 h to complete combustion and finally annealed at 800 ºC for 3 h to enhance crystallinity.

Fabrication of electrodes: For electrode preparation, the nickel foil used as a current collector was ultrasonically cleaned in a solution (4 mL HCl + 50 mL deionised water) for 5 min and then in ethanol, acetone and deionised water for 30 min each and subsequently dried overnight at 70 ºC. The working electrode was fabricated by mixing 80 wt.% of the active material ($Ni_xZn_{1-x}Fe_2O_4$ (x = 0, 0.3, 0.5)), 10 wt.% of PVDF as a binder, 10 wt.% of activated carbon as a conducting additive and a few drops of NMP to prepare a homogeneous slurry. The slurry was uniformly coated by the drop-casting method onto a 1 cm × 1 cm area of nickel foil and subsequently dried at 80 ºC overnight to obtain the working electrode. The mass of all working electrodes ($Ni_xZn_{1-x}Fe_2O_4$, x = 0, 0.3, 0.5) was ~8 mg.

Characterisation: The crystalline phases of $Ni_xZn_{1-x}Fe_2O_4$ (x = 0, 0.3, 0.5) were identified *via* powder X-ray diffraction (XRD, Rigaku MiniFlex 600) over a 2θ range of 15-80º. Surface morphology and elemental distribution were analysed using field-emission scanning electron microscopy (FESEM, Carl Zeiss Gemini) coupled with energy-dispersive X-ray spectroscopy (EDX, Bruker Nanoflash). Chemical states and elemental compositions were determined by X-ray photoelectron spectroscopy (XPS, Thermo-Fisher Nexsa) using an Al*K*α source. Molecular vibrations and functional groups were characterised *via* Fourier-transform infrared spectroscopy (FTIR, Perkin-Elmer Spectrum Two) in the 4000-400 cm^{-1} range. Confocal Raman microscopy (WiTec Alpha 300, 532 nm laser) was employed to probe M-O vibrations, specifically focusing on the 4000-50 cm^{-1} region. The optical properties and bandgap values were derived from UV-Vis absorbance spectra (Agilent Cary 60). Electrochemical measurements of $Ni_xZn_{1-x}Fe_2O_4$ (x = 0, 0.3, 0.5) electrodes were conducted using a VSP Biologic electrochemical workstation in a three-electrode configuration. The prepared electrode served as the working electrode, a platinum wire and an Ag/AgCl electrode acted as a counter electrode and a reference electrode, respectively. A 2 M Na_2SO_4 aqueous solution acted as the electrolyte and all measurements were conducted at room temperature.

RESULTS AND DISCUSSION

PXRD analysis: The powder X-ray diffraction (PXRD) patterns of the $Ni_xZn_{1-x}Fe_2O_4$ (x = 0, 0.3, 0.5) nanoparticles are shown in Fig. 1. All diffraction peaks correspond to the

characteristic reflections of a single-phase cubic spinel structure (space group $Fd\bar{3}m$), indexed to the (111), (220), (311), (222), (400), (422), (511) and (440) planes according to JCPDS card No. 10-0325. The strong and sharp (311) reflection signifies high crystallinity and complete phase formation. No impurity peaks were detected, confirming successful incorporation of Ni into the $ZnFe_2O_4$ system [29].

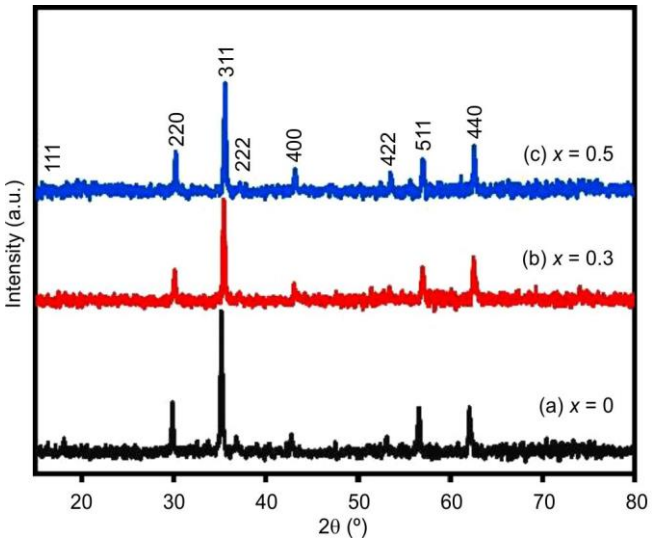

Fig. 1. PXRD spectra of $Ni_xZn_{1-x}Fe_2O_4$ (x = 0, 0.3, 0.5)

The average crystallite size (D) was estimated using the Debye-Scherrer's equation:

$$D = \frac{k\lambda}{\beta\cos\theta}$$

where, k = 0.9, λ = 1.5406 Å (Cu$K\alpha$); β is the full width at half maximum (FWHM) and θ is the Bragg angle.

The lattice parameter (a) for the cubic system was calculated from Bragg's law using the (311) reflection:

$$a = d\sqrt{h^2 + k^2 + l^2}$$

The unit cell volume (V) follows the cubic relationship:

$$V = a^3$$

The X-ray density (ρ_x) was evaluated using:

$$\rho_x = \frac{ZM}{N_A V}$$

where Z = 8 is the number of formula units per unit cell, M is the molecular weight and N_A is Avogadro's number.

The dislocation density (δ) was determined from:

$$\delta = \frac{1}{D^2}$$

and the lattice strain (ε) was estimated by:

$$\varepsilon = \frac{\beta}{4\tan\theta}$$

Table-1 shows that with increasing Ni content, the values of average crystallite size (D), lattice parameter (a) and unit cell volume (V) decrease, while the values of X-ray density (ρ_x), dislocation density (δ) and lattice strain increase [30]. These variations indicate subtle structural changes arising from Ni incorporation into the $ZnFe_2O_4$ lattice, leading to the moderate lattice distortion and defect formation while maintaining the stable spinel phase. Such structural changes are beneficial for the electrochemical applications as they enhance specific capacitance and rate capability by providing additional active sites and facilitating ion transport pathways.

UV-vis studies: The UV-visible absorption spectra and corresponding Tauc plots of $Ni_xZn_{1-x}Fe_2O_4$ (x = 0, 0.3, 0.5) nanoparticles, recorded at room temperature (Fig. 2), were analysed to estimate the optical band gap energies. The band gap values were determined from the linear extrapolation of $(\alpha h\nu)^{1/2}$ *versus* hν, assuming an indirect allowed transition. The estimated band gap energies decrease from 1.84 eV (x = 0) to 1.60 eV (x = 0.3) and 1.54 eV (x = 0.5) [31]. The observed band gap narrowing can be attributed to the incorporation of Ni^{2+} ions into the $ZnFe_2O_4$ lattice, which introduces additional electronic states within the band structure and may facilitate charge carrier transport. Although UV-Vis spectroscopy provides indirect evidence of improved electronic conductivity, the reduced band gap suggests enhanced electron mobility that can contribute to improved electrochemical redox activity. These features make nickel-substituted zinc ferrite a promising electrode material for high-performance supercapacitor applications.

XPS studies: X-ray photoelectron spectroscopy was employed to analyse the surface elemental composition, oxidation

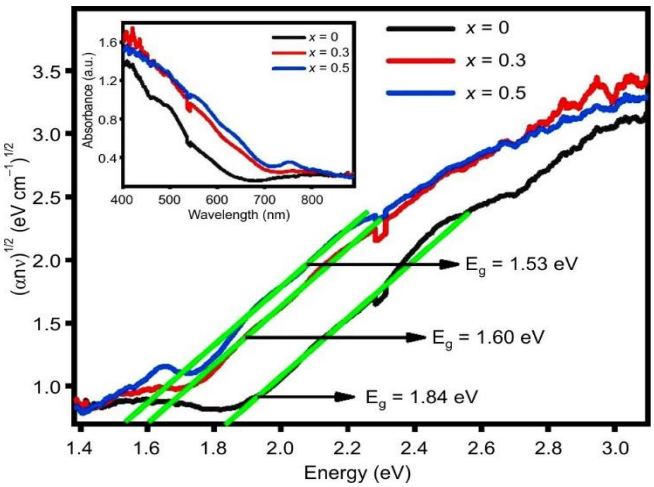

Fig. 2. Absorption spectra and their Tauc plots of $Ni_xZn_{1-x}Fe_2O_4$ (x = 0. 0.3, 0.5) by UV-vis analysis

TABLE-1
PARAMETERS OBTAINED FROM XRD SPECTRA OF $Ni_xZn_{1-x}Fe_2O_4$ (x = 0. 0.3, 0.5), RESPECTIVELY

$Ni_xZn_{1-x}Fe_2O_4$	D (nm)	a (Å)	V (Å^3)	X_d (g cm^{-3})	δ (10^{14} m^{-2})	ε (10^{-3})
x = 0	39.74	8.458	605.2	5.29	6.33	3.02
x = 0.3	38.23	8.403	593.3	5.35	6.84	3.12
x = 0.5	36.06	8.366	585.6	5.39	7.69	3.29

states and chemistry environment of the $Ni_xZn_{1-x}Fe_2O_4$ (x = 0, 0.3, 0.5) samples [32]. The survey spectrum (Fig. 3a) confirms the $ZnFe_2O_4$ system and the high-resolution Zn 2p spectrum (Fig. 3b) displays Zn $2p_{3/2}$ and Zn $2p_{1/2}$ peaks at approximately 1021 and 1044 eV, respectively, characteristic of Zn^{2+} in tetrahedral coordination. The Fe 2p spectrum (Fig. 3c) shows the Fe $2p_{3/2}$ and Fe $2p_{1/2}$ peaks at ~711 and 725 eV, along with weak satellite features, confirming Fe^{3+} as dominant oxidation state. The O 1s peak (Fig. 3d) can be resolved into components corresponding to lattice oxygen (~529 eV), surface oxygen species (~532 eV) and adsorbed molecular species (~533 eV). The C 1s peak (Fig. 3e) at 284.6 eV arises from adventitious carbon and was used for charge calibration [33].

For the Ni-substituted sample (x = 0.3), the survey spectrum (Fig. 4a) shows the emergence of Ni 2p peaks, confirming successful incorporation of Ni into the Zn ferrite matrix. The Ni 2p spectrum (Fig. 4b) exhibits Ni $2p_{3/2}$ at ~855 eV and Ni $2p_{1/2}$ near ~874 eV, accompanied by a characteristic satellite feature around 861 eV, consistent with Ni^{2+} in an octahedral oxide environment. The Zn 2p (Fig. 4c) and Fe 2p (Fig. 4d) spectra remain at energies typical of Zn^{2+} and Fe^{3+}, indicating that Ni substitution does not alter their oxidation states. The O 1s spectrum (Fig. 4e) contains lattice oxygen (~530 eV) and surface-chemisorbed oxygen (~532 eV), with slightly increased intensity relative to x = 0, suggesting a higher concentration of surface oxygen species [34,35].

At higher Ni content (x = 0.5), the survey spectrum (Fig. 5a) displays prominent Ni 2p features along with Zn, Fe, O and C peaks, confirming a Ni-rich ferrite composition without secondary phases. The high-resolution Ni 2p spectrum (Fig. 5b) reveals two Ni $2p_{3/2}$ components at ~853.4 eV and ~855.4 eV corresponding to Ni^{2+} and Ni^{3+}, respectively, together with a strong satellite peak near 861 eV. The presence of mixed-valent Ni^{2+}/Ni^{3+} indicates increased redox flexibility, which is beneficial for pseudocapacitive behaviour. The Zn 2p (Fig. 5c) and Fe 2p (Fig. 5d) spectra remain unchanged, confirming Zn^{2+} and Fe^{3+} as stable oxidation states across all compositions. The O 1s spectrum (Fig. 5e) shows lattice oxygen (~529 eV), defect-related oxygen (~530–531 eV) and surface hydroxyl/adsorbed species (~533 eV), with the defect-related peak more pronounced in the Ni-rich sample, indicating a greater concentration of oxygen vacancies. The C 1s spectrum (Fig. 5f) exhibits C–C, C–O and carbonate contributions typical of surface contamination [36].

In $ZnFe_2O_4$, since Zn^{2+} ions occupy tetrahedral sites and Fe^{3+} ions occupy octahedral sites, charge transport occurs *via* Fe^{3+}/Fe^{2+} hopping. The substitution of Zn^{2+} with the smaller Ni^{2+} cation facilitates a strong preference for octahedral occupancy driven by its high crystal field stabilisation energy (CFSE), which induces a slight lattice contraction and introduces active Ni^{2+}/Ni^{3+} redox couples. This reconfiguration engenders a synergistic effect wherein both nickel and iron ions contribute to the Faradaic pseudocapacitive charge storage. This creates multiple hopping pathways (Fe–Fe, Fe–Ni, Ni–Ni) and strengthens orbital overlap with oxygen, reducing the electron transport barrier [31,37]. These electronic reconfi-

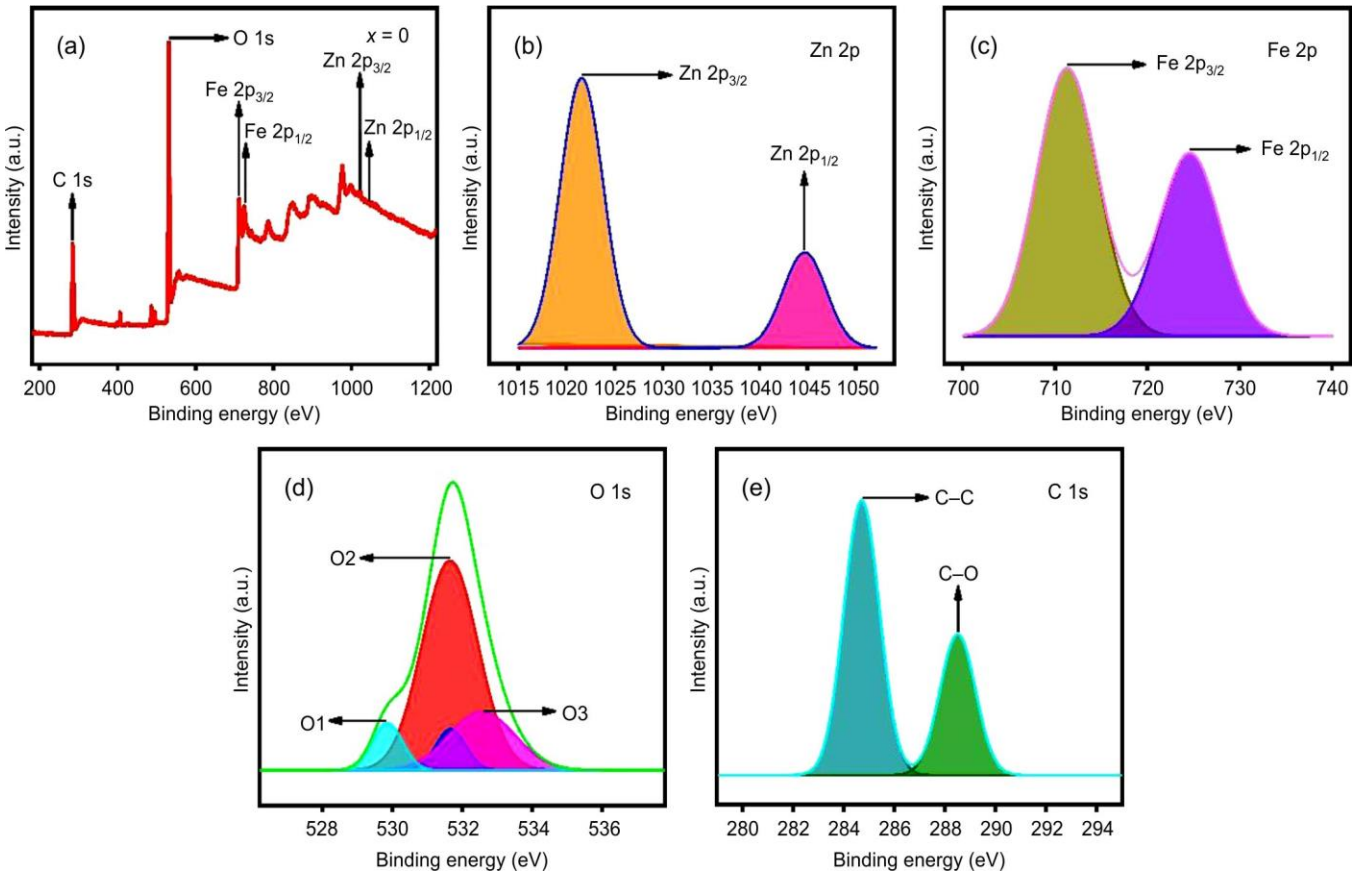

Fig. 3a-e. XPS spectra of $Ni_xZn_{1-x}Fe_2O_4$ (x = 0)

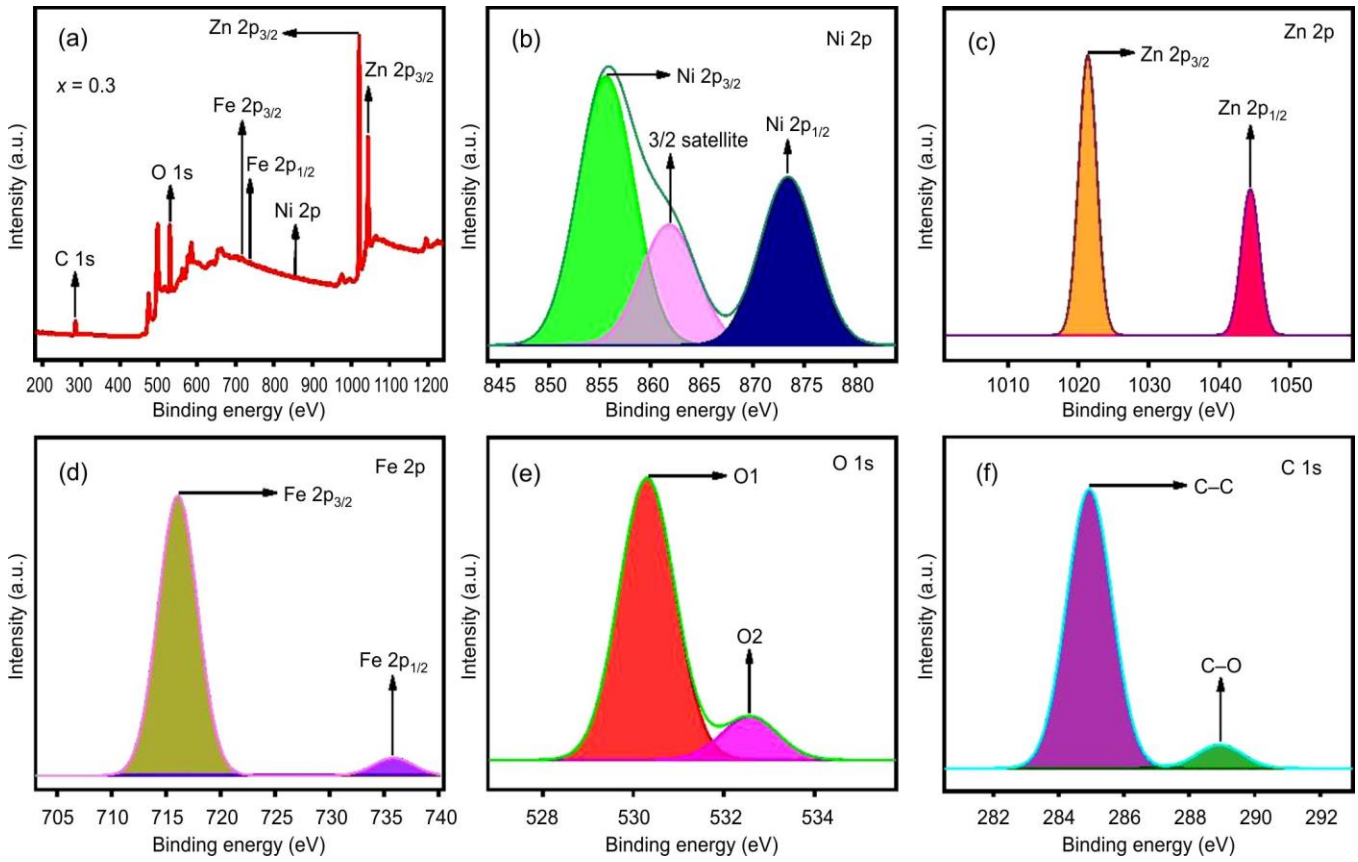

Fig. 4a-f. XPS spectra of $Ni_xZn_{1-x}Fe_2O_4$ (x = 0.3)

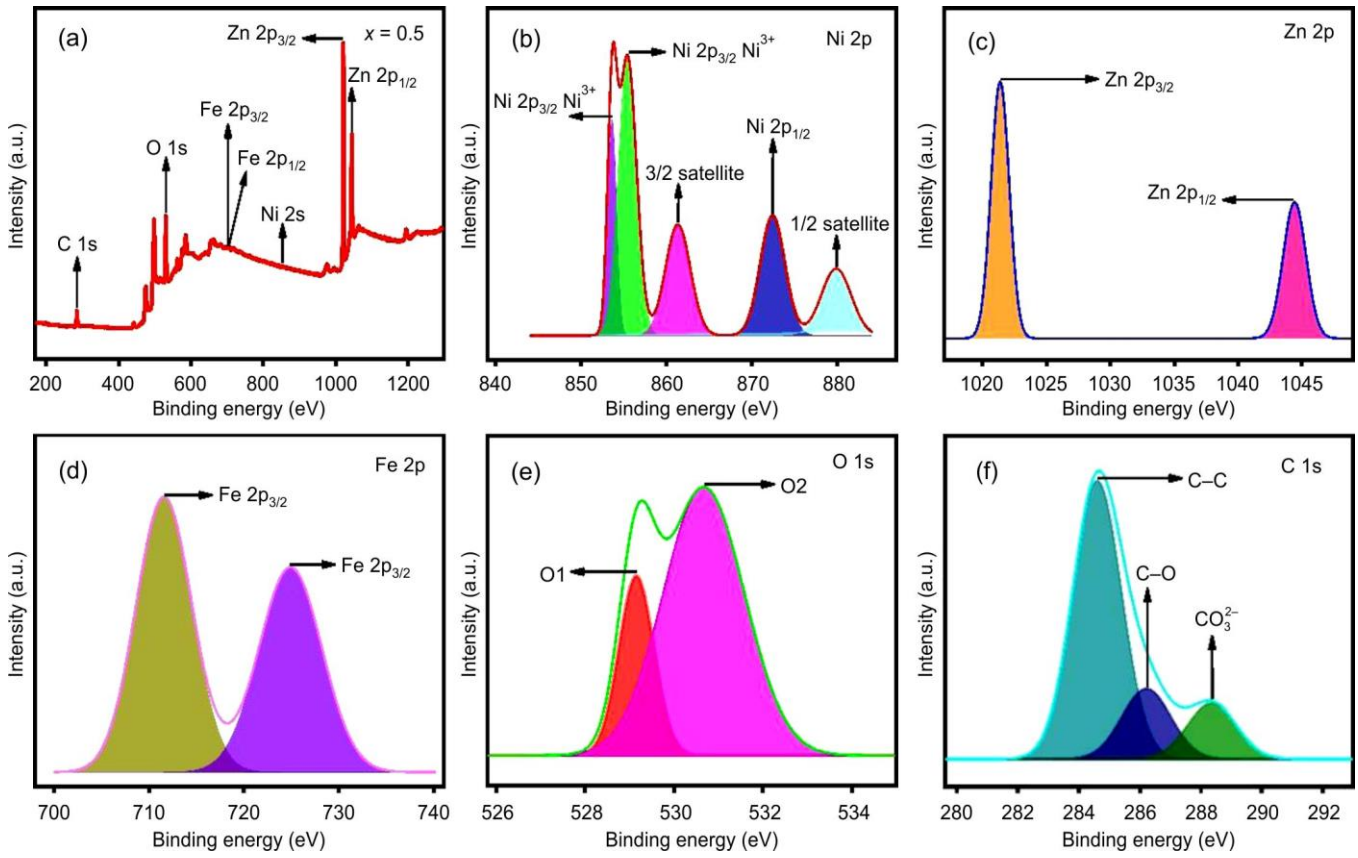

Fig. 5a-f. XPS spectra of $Ni_xZn_{1-x}Fe_2O_4$ (x = 0.5)

gurations are typically accompanied by the lattice distortion, increased spinel inversion and oxygen-vacancy formation. Thus, these structural modifications broaden the electronic bandwidth, narrow the band gap and promote rapid ion diffusion, making spinel ferrites attractive for enhanced energy storage.

FTIR studies: As shown in Fig. 6, the FTIR spectra of $Ni_xZn_{1-x}Fe_2O_4$ (x = 0, 0.3, 0.5) compounds exhibit two characteristic absorption bands that confirm the formation of the spinel ferrite structure. The high-frequency band (ν_1) appears between 524 and 539 cm^{-1} in the tetrahedral sites, while the weaker low-frequency band (ν_2) is observed between 405.84 and 416.84 cm^{-1} in the octahedral sites. These bands result from the M–O stretching vibrations of the spinel ferrite; the values are listed in Table-2 [29]. The slight shifts in these bands with increasing nickel content indicate changes in the M–O bonding environment and cation distributions within the spinel ferrite structure. These modifications may enhance the redox-active sites, potentially improving the material's supercapacitive performance.

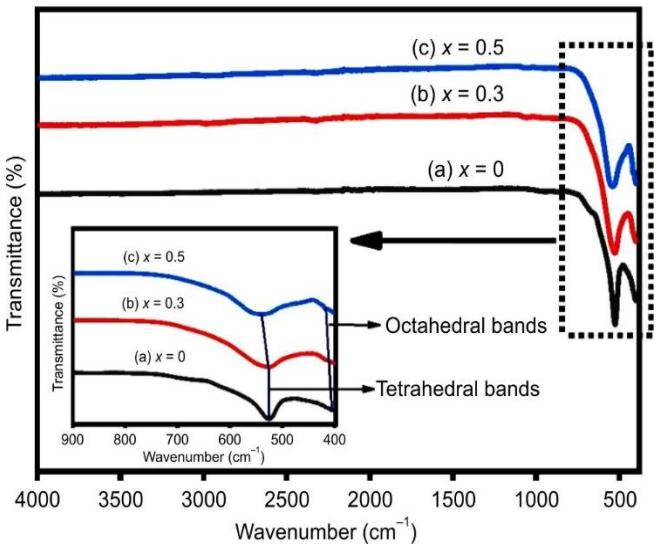

Fig. 6. FTIR spectra of $Ni_xZn_{1-x}Fe_2O_4$ (x = 0. 0.3, 0.5)

TABLE-2
M-O BANDS AT TETRAHEDRAL AND OCTAHEDRAL SITE VALUES OF $Ni_xZn_{1-x}Fe_2O_4$(x = 0. 0.3, 0.5)

$Ni_xZn_{1-x}Fe_2O_4$	Tetrahedral band υ_1 (cm^{-1})	Octahedral band υ_2 (cm^{-1})
x = 0	525.43	405.51
x = 0.3	526.51	410.94
x = 0.5	539.50	416.59

Raman spectral studies: Fig. 7 shows the Raman spectra of $Ni_xZn_{1-x}Fe_2O_4$ (x = 0, 0.3, 0.5) nanoparticles, exhibiting five distinct vibrational modes: The A_{1g} mode corresponds to symmetric M–O stretching at the tetrahedral sites. The $T_{2g}(3)$ and $T_{2g}(2)$ modes, are associated with asymmetric vibrations at tetrahedral and octahedral sites, respectively. The lower-frequency $T_{2g}(1)$ mode arises from symmetric bending at octahedral sites, while the E_g mode represents coupled bending vibrations of both sites. The Raman modes listed in Table-3 confirm the successful formation of the spinel phase [34,38].

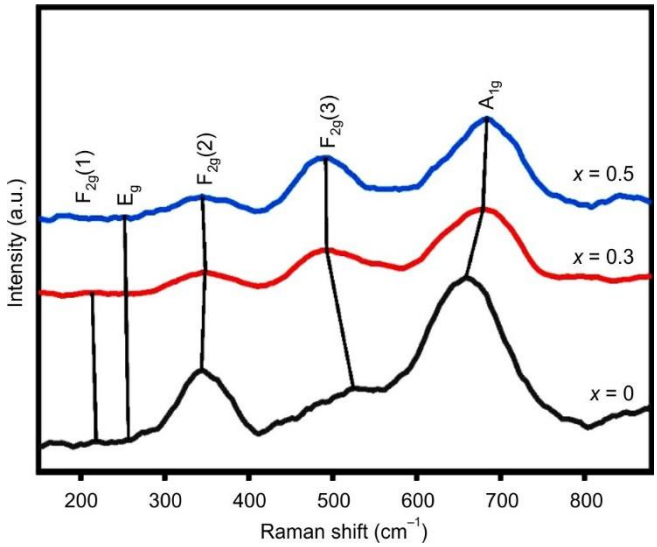

Fig. 7. Raman spectra for $Ni_xZn_{1-x}Fe_2O_4$ (x = 0. 0.3, 0.5)

The progressive shifts in these bands indicate lattice distortion induced by Ni incorporation, which can significantly influence electrochemical behaviour and enhance supercapacitor performance by facilitating electron hopping and improving redox activity.

TABLE-3
RAMAN ACTIVE MODES' VALUES OF $Ni_xZn_{1-x}Fe_2O_4$ (x = 0, 0.3, 0.5), RESPECTIVELY

$Ni_xZn_{1-x}Fe_2O_4$	$F_{2g}1$ (cm^{-1})	E_g (cm^{-1})	$F_{2g}2$ (cm^{-1})	$F_{2g}3$ (cm^{-1})	A_{1g} (cm^{-1})
x = 0	220.13	256.61	344.34	524.84	660.20
x = 0.3	214.26	–	347.37	492.04	680.66
x = 0.5	–	250.74	345.77	487.77	683.69

FE-SEM studies: The FESEM images of $Ni_xZn_{1-x}Fe_2O_4$ (x = 0, 0.3, 0.5) reveal aggregates of nearly spherical nanoparticles with moderate clustering (Fig. 8a-c). Particle-size distributions were obtained from the corresponding histograms in Fig. 8d-f using ImageJ analysis. The average particle sizes are 48.02 nm (σ = 1.26 nm), 43.75 nm (σ = 1.47 nm) and 41.21 nm (σ = 1.35 nm) for x = 0, 0.3 and 0.5, respectively, indicating narrow and nearly monodisperse size distributions. A consistent decrease in particle size with increasing Ni content agrees well with the crystallite sizes estimated from XRD (39.74 to 36.06 nm). The slightly larger FESEM particle sizes compared to XRD-derived crystallite sizes suggest that the particles are composed of multiple crystallites. The Ni-rich sample (x = 0.5) provides a larger specific surface area and an improved number of electroactive sites, contributing to the enhanced capacitive performance observed electrochemically.

EDX studies: The elemental composition and distribution of $Ni_xZn_{1-x}Fe_2O_4$ (x = 0, 0.3, 0.5) nanoparticles were verified using energy-dispersive X-ray spectroscopy (EDX). The spectra (Fig. 9a-c) show the presence of Ni signals along with Zn, Fe and O, without any additional peaks, confirming high phase purity. The quantitative analysis reveals the elemental ratios in close agreement with the nominal stoichiometry. Furthermore, elemental mapping revealed a uniform spatial distribution of all constituent cations, showing Ni incorporation with-

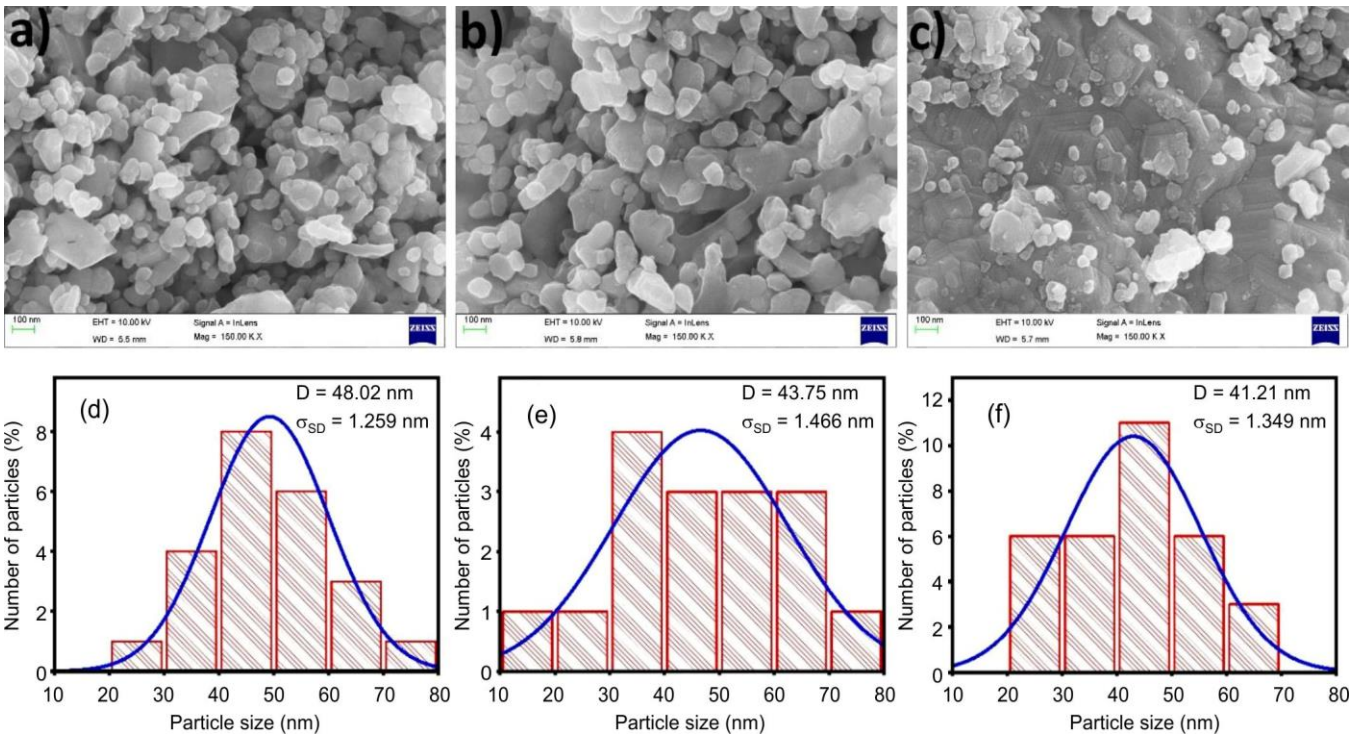

Fig. 8. FESEM analysis of $Ni_xZn_{1-x}Fe_2O_4$ (x = 0, 0.3, 0.5) (a-c) morphological image in 100 nm, (d-f) and their corresponding histograms, respectively

out phase segregation. Fig. 10 demonstrates the uniform elemental distribution and stoichiometric stability by clearly showing a gradual increase in Ni content and a corresponding decrease in Zn content as x increases.

Electrochemical analysis

Cyclic voltammetry (CV) studies: The cyclic voltammograms of $Ni_xZn_{1-x}Fe_2O_4$ (x = 0, 0.3, 0.5) electrodes at scan rates of 5-50 mV s^{-1} (Fig. 11a-c) showed a regular evolution caused by increasing Ni content. All samples had quasi-rectangular CV profiles with considerable redox contributions, indicating pseudocapacitive charge-storage behaviour. The specific capacitance was calculated using the relation:

$$C_s = \frac{\int IdV}{2\ m\ s\ \Delta V}$$

where, ∫IdV corresponds to the integrated area of CV curve; m is the mass of the active material; s is the scan rate and ΔV is the applied potential window [21]. The calculated capacitance values are summarised in Table-4 and their variation with scan rate is illustrated in Fig. 11d. At lower scan rates (5 mV s^{-1}), the electrolyte ions have sufficient time to diffuse deeply into the electrode, resulting in enhanced charge storage. In contrast, at higher scan rates (50 mV s^{-1}), although the CV area increases, the specific capacitance decreases due to the restricted ion diffusion. Among the samples, $ZnFe_2O_4$ (x = 0) and the low Ni-substituted sample (x = 0.3) at 5 mV s^{-1} show low current responses and small CV areas, suggesting weak capacitive behaviour with minimal redox activity. The x = 0.5 composition exhibits the largest CV area at 5 mV s^{-1}, indicating superior charge-storage capability. This enhancement arises from the additional Ni^{2+}/Ni^{3+} redox transitions, which improve electronic conductivity and promote faster Faradaic reactions. These findings demonstrate that $Ni_{0.5}Zn_{0.5}Fe_2O_4$ ferrites possesses favourable electrochemical kinetics and is a promising candidate for the high-performance supercapacitor applications.

GCD analysis: Fig. 12a-c display the galvanostatic charge–discharge (GCD) profiles of the $Ni_xZn_{1-x}Fe_2O_4$ (x = 0, 0.3, 0.5) electrodes measured at current densities from 1 to 5 A g^{-1}. All samples exhibit quasi-triangular curves with slight deviations from linearity, characteristic of pseudocapacitive charge storage [39]. At lower current densities, electrolyte ions can penetrate more effectively into the electrode, resulting in the longer discharge times, whereas at higher current densities, limited ion accessibility leads to shorter discharge profiles. The specific capacitance (C_s) was obtained using:

$$C_s = \frac{I\Delta t}{m\Delta v}$$

where I is the applied current, Δt is the discharge time; m is the mass of active material; and ΔV is the voltage window [21]. The obtained capacitance values for all compositions are listed in Table-5 and their variation with current density is illustrated in Fig. 12d. As shown in Fig. 12d, the specific

TABLE-4
SPECIFIC CAPACITANCE OF ALL SAMPLES AT DIFFERENT SCAN RATES THROUGH CV CURVES

$Ni_xZn_{1-x}Fe_2O_4$	mV s^{-1} (F g^{-1})				
	5	10	15	25	50
x = 0	60.2	49.0	43.7	36.2	28.8
x = 0.3	90.2	63.9	53.9	43.1	34.4
x = 0.5	174.1	116.5	85.8	62.5	32.4

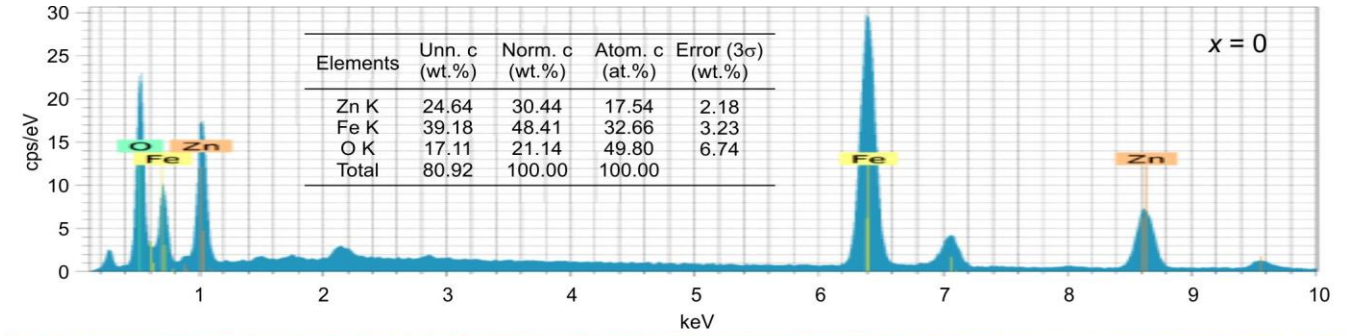

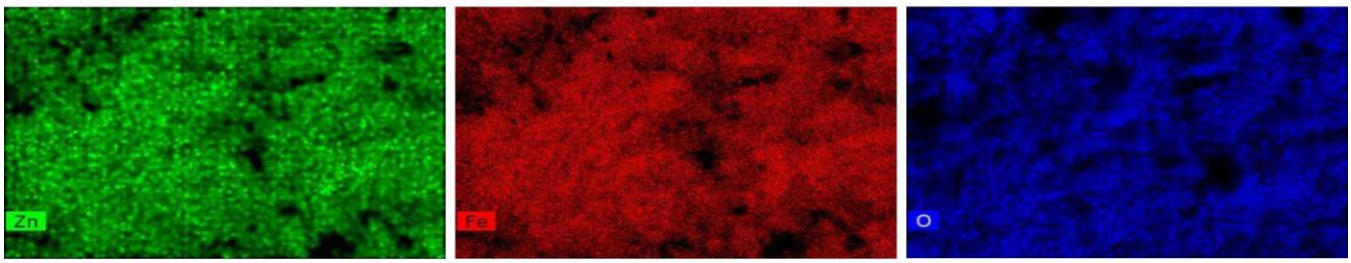

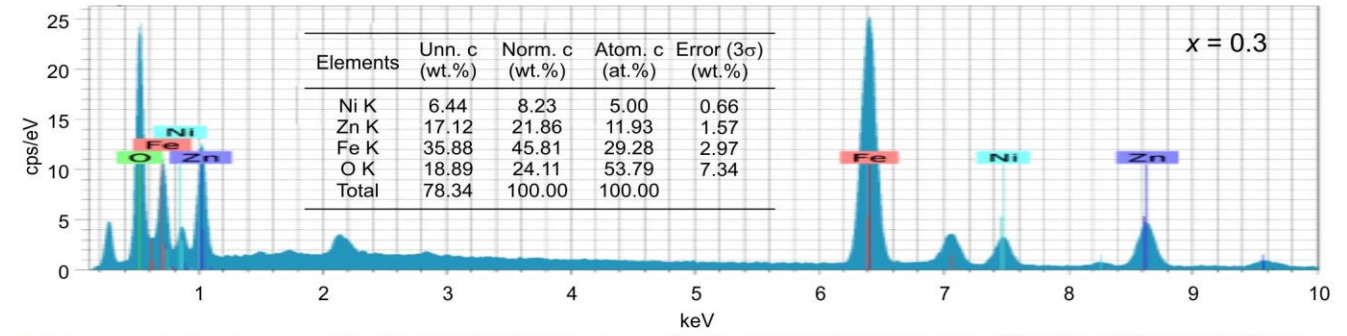

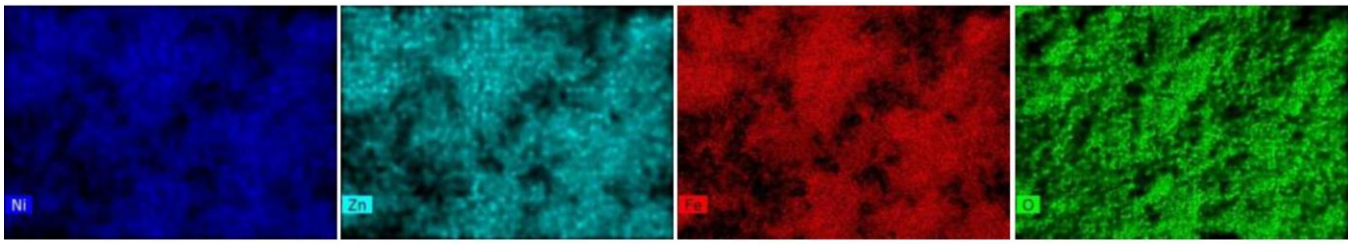

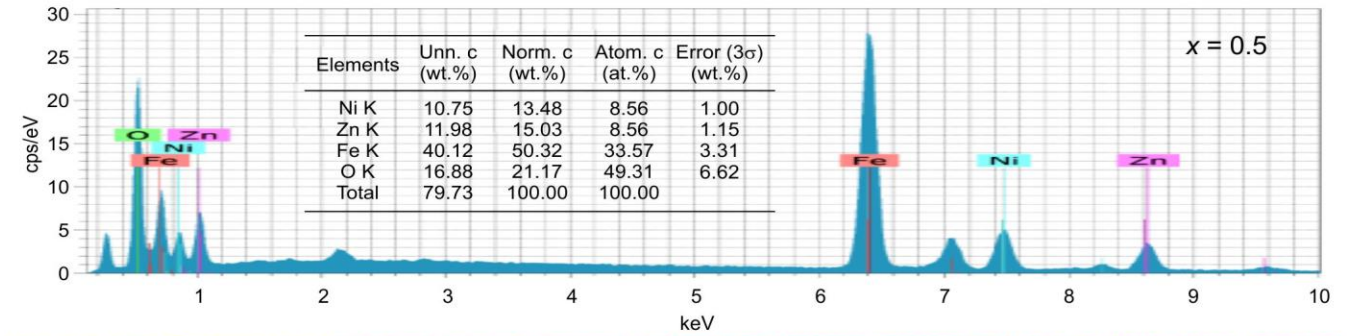

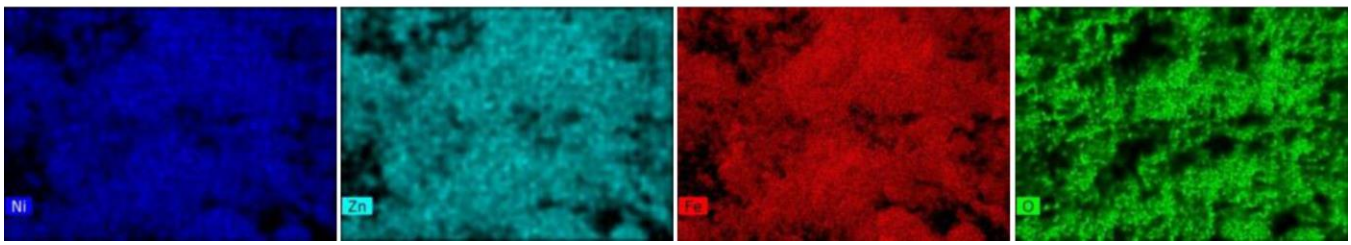

Fig. 9. EDX analysis of elemental composition and elemental mapping of $Ni_xZn_{1-x}Fe_2O_4$ (x = 0, 0.3, 0.5)

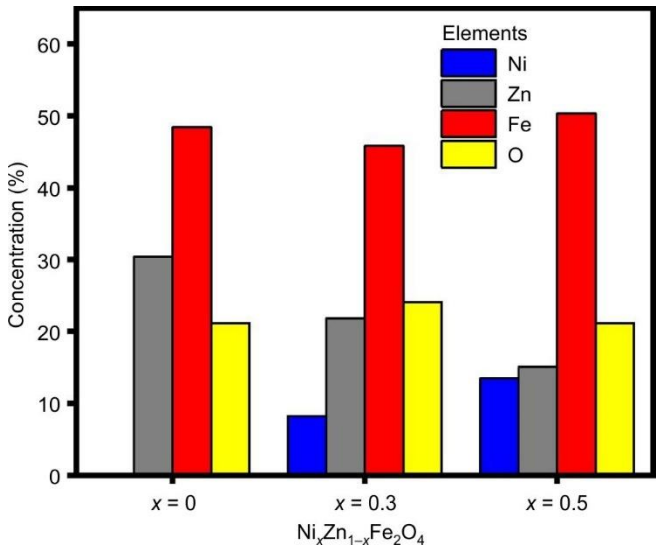

Fig. 10. Bar chart of the elemental concentration of $Ni_xZn_{1-x}Fe_2O_4$ (x = 0, 0.3, 0.5)

TABLE-5
SPECIFIC CAPACITANCES OF ALL MATERIALS AT DIFFERENT CURRENT DENSITIES *via* GCD CURVES

$Ni_xZn_{1-x}Fe_2O_4$	A g^{-1} (F g^{-1})				
	1	2	3	4	5
x = 0	98.1	78.4	60.6	44.1	30.9
x = 0.3	202.5	177.5	132.0	92.5	61
x = 0.5	251.0	194.3	143.6	118.2	78.6

capacitance at 1 A g^{-1} increases markedly with Ni substitution, with the $Ni_{0.5}Zn_{0.5}Fe_2O_4$ electrode delivering the highest value. Its extended discharge profile and more pronounced nonlinearity reflect enhanced redox activity, improved electron-transport pathways and more efficient ion diffusion resulting from Ni incorporation.

Electrochemical impedance spectroscopy (EIS): The EIS was employed to investigate the charge-transfer and ion-diffusion characteristics of the $Ni_xZn_{1-x}Fe_2O_4$ (x = 0, 0.3, 0.5) electrodes over the frequency range of 0.1 Hz to 100 kHz. The Nyquist plots (Fig. 13) exhibit a small high-frequency inter-

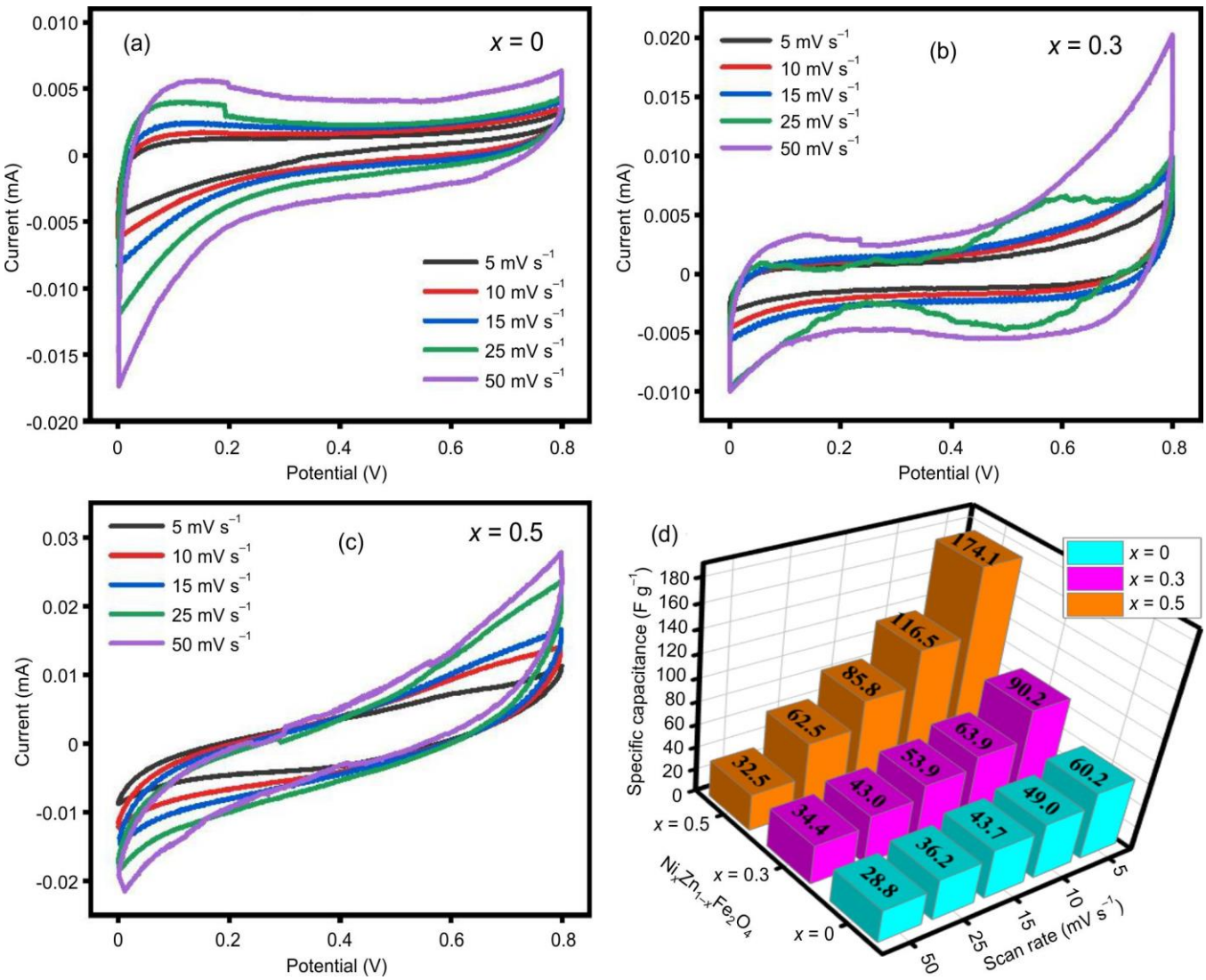

Fig. 11. CV studies of $Ni_xZn_{1-x}Fe_2O_4$ electrodes at different scan rates (a) x = 0, (b) x = 0.3, (c) x = 0.5, (d) 3D Bar chart for all sample's specific capacitances

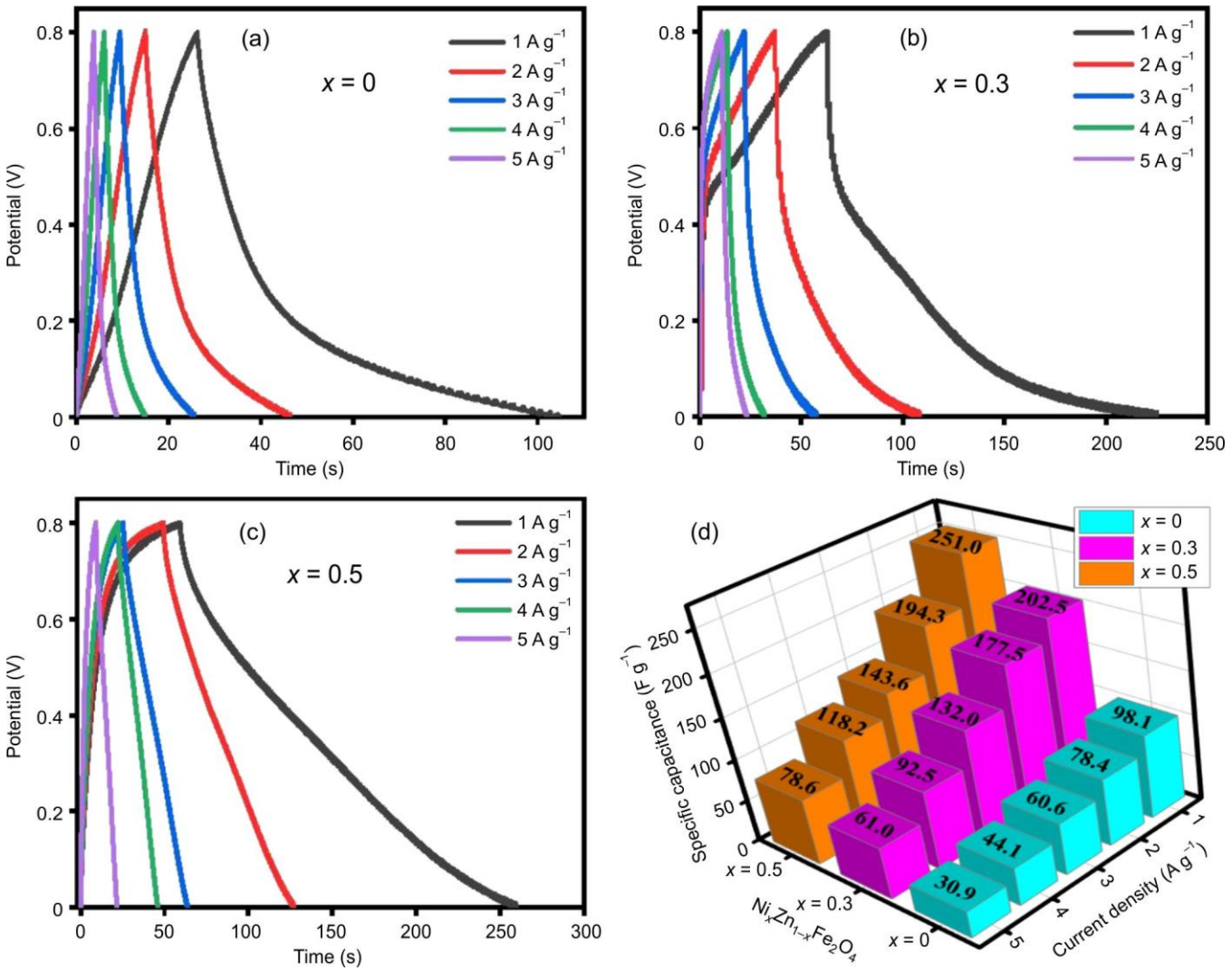

Fig. 12. GCD studies of $Ni_xZn_{1-x}Fe_2O_4$ electrodes at different current densities (a) x = 0, (b) x = 0.3, (c) x = 0.5, (d) 3D Bar chart for all sample's specific capacitances

cept corresponding to the solution resistance (R_s), followed by a depressed semicircle that represents the charge-transfer resistance (R_{ct}). The extended sloping line in the low-frequency region reflects Warburg impedance associated with ion diffusion and confirms the pseudocapacitive behaviour of the electrodes [40]. The extracted R_{ct} values for x = 0, 0.3 and 0.5 are 0.25 Ω, 0.21 Ω and 0.11 Ω, respectively, demonstrating a progressive reduction with increasing Ni content. The substantially lower R_{ct} of the $Ni_{0.5}Zn_{0.5}Fe_2O_4$ electrode signifies more efficient charge-transfer kinetics and enhanced electronic conductivity, which facilitate rapid Faradaic reactions and improved ion transport at the electrode–electrolyte interface. These characteristics directly contribute to the superior electrochemical performance observed for the Ni-rich compositions in CV and GCD analyses.

Energy density and power density: The energy and power density characteristics of the $Ni_xZn_{1-x}Fe_2O_4$ (x = 0, 0.3, 0.5) electrodes were evaluated to assess their suitability for the high-performance supercapacitor applications. The energy density (E) and power density (P) were calculated using the following relations:

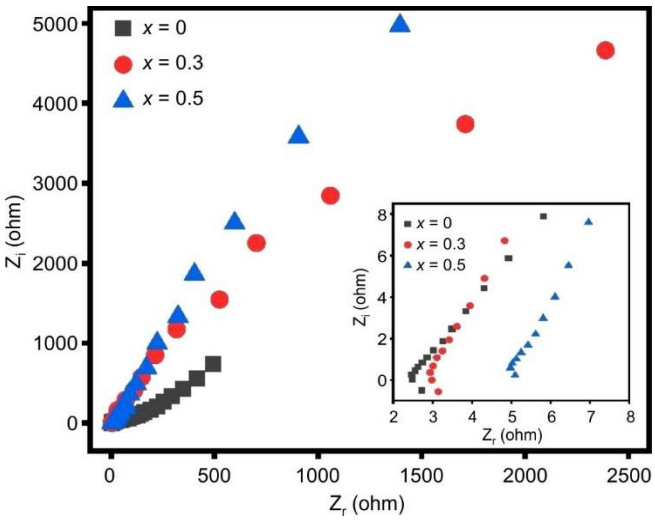

Fig. 13. Nyquist plots for $Ni_xZn_{1-x}Fe_2O_4$ (x = 0, 0.3, 0.5)

$$E = \frac{1}{2}\frac{C \times \Delta V^2}{3.6}$$

$$P = \frac{E \times 3600}{t}$$

where E is energy density (Wh kg^{-1}); C is the specific capacitance from GCD curves (F g^{-1}); ΔV potential window (V); P is the power density (W kg^{-1}) and t is the discharge time (s) [41]. The calculated values are shown in Fig. 14 as a Ragone plot. The Ni-containing electrodes exhibits significantly enhanced energy densities compared to pristine $ZnFe_2O_4$. At 1 A g^{-1}, the energy densities for x = 0, 0.3 and 0.5 are 8.72, 18.0 and 22.31 Wh kg^{-1}, respectively, demonstrating the strong influence of Ni incorporation on improving charge-storage capability. All samples at 1 A g^{-1} deliver comparable power densities (~400 W kg^{-1}) indicating that the enhanced energy density of the Ni-rich compositions does not compromise their high-rate performance.

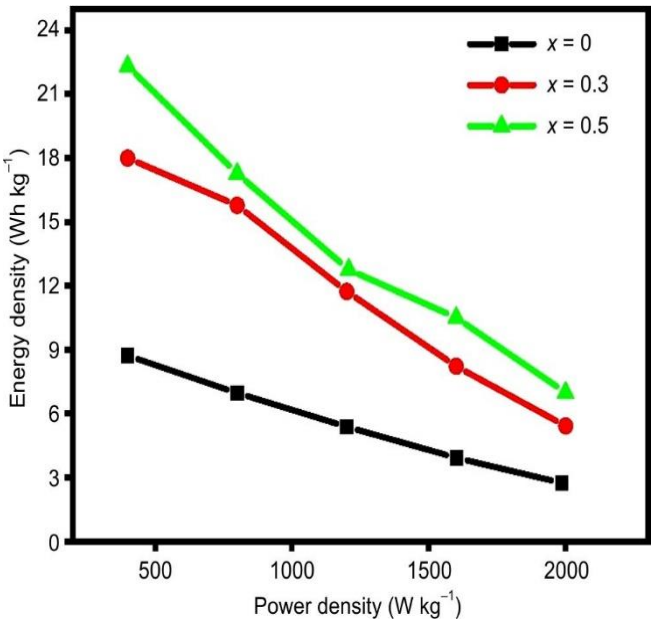

Fig. 14. Ragone plot for $Ni_xZn_{1-x}Fe_2O_4$ (x = 0, 0.3, 0.5)

Cyclic stability test: The cycling stability of $Ni_xZn_{1-x}Fe_2O_4$ (x = 0, 0.3, 0.5) electrodes was evaluated over 200 cycles at 4 A g^{-1} (Fig. 15). The undoped sample (x = 0) retains about 87% of its initial capacitance, whereas Ni-substituted samples show improved stability, with x = 0.3 and x = 0.5 retaining approximately 92% and 91.54%, respectively. The improved cycling behaviour in Ni-substituted samples can be attributed to enhanced redox activity and better charge transport arising from the incorporation of Ni^{2+} ions into the spinel lattice. These results confirm that Ni substitution plays a significant role in improving the long-term electrochemical stability of $ZnFe_2O_4$ based electrodes.

Comparative studies: Table-6 presents a comparative data of the electrochemical performance of the $Ni_{0.5}Zn_{0.5}Fe_2O_4$ electrode with previously reported carbon-based and ferrite-based supercapacitor materials. As shown, mostly reported electrodes exhibit specific capacitance values below 250 F g^{-1} under comparable experimental conditions, with relatively limited energy density. $Ni_{0.5}Zn_{0.5}Fe_2O_4$ electrode developed in this work delivers a specific capacitance of 250 F g^{-1} at a

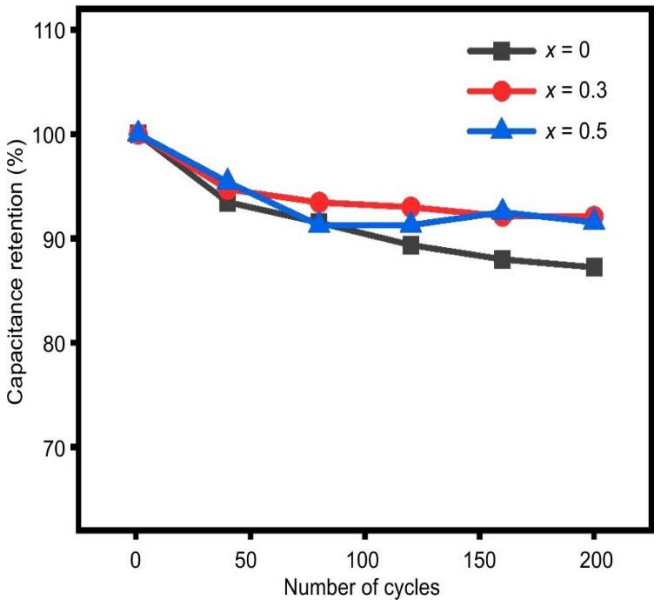

Fig. 15. Cyclic stability plots (200 cycles at 4 A g^{-1}) plot for $Ni_xZn_{1-x}Fe_2O_4$ (x = 0, 0.3, 0.5)

current density of 1 A g^{-1}, along with an energy density of 22.31 Wh kg^{-1} and a power density of 400 W kg^{-1}. These values are comparable to and in several cases exceed, those of previously reported ferrite-based electrodes. These results demonstrate that Ni-substituted $ZnFe_2O_4$ is a promising electrode material for advanced electrochemical energy storage applications.

Conclusion

$Ni_xZn_{1-x}Fe_2O_4$ (x = 0, 0.3 and 0.5) nanoferrites were successfully synthesised *via* a sol-gel auto combustion method to investigate the influence of Ni substitution on the structural and electrochemical properties of $ZnFe_2O_4$. The structural and spectroscopic characterisation (XRD, FTIR, Raman, UV-vis, XPS and EDX) confirmed the formation of a pure cubic spinel phase and revealed Ni-induced lattice modifications accompanied by a reduced band gap. FESEM analysis showed particle-like morphologies with moderate clusters that favour electrolyte penetration and enhanced electrochemical activity. Electrochemical studies demonstrated that Ni substitution significantly improves the pseudocapacitive behaviour, charge-transfer characteristics, and ion diffusion kinetics. Among the investigated compositions, the $Ni_{0.5}Zn_{0.5}Fe_2O_4$ electrode exhibited the best performance, delivering a high specific capacitance of 250 F g^{-1} at 1 A g^{-1}, together with an energy density of 22.31 Wh kg^{-1} and a power density of 400 W kg^{-1}. In addition, the $Ni_{0.5}Zn_{0.5}Fe_2O_4$ electrode retained 91.54% of its initial capacitance after 200 cycles, indicating reasonable cycling stability. These findings demonstrate that Ni substitution is an effective strategy for enhancing the electrochemical performance of $ZnFe_2O_4$, making $Ni_{0.5}Zn_{0.5}Fe_2O_4$ a promising electrode material for high-performance supercapacitor applications.

ACKNOWLEDGEMENTS

The authors sincerely acknowledge the Department of Physics, Mr. S. Sivaraj, Department of Physics, Government

TABLE-6
COMPARATIVE ELECTROCHEMICAL PERFORMANCE OF $Ni_{0.5}Zn_{0.5}Fe_2O_4$ AND PREVIOUSLY REPORTED CARBON-BASED AND FERRITE-BASED SUPERCAPACITOR MATERIALS

Materials	Specific capacitance ($F\ g^{-1}$)	Energy density ($Wh\ kg^{-1}$)	Power density ($W\ kg^{-1}$)	Capacitance retention	Ref.
$MnFe_2O_4$	190 at 2 mV s^{-1}	–	–	–	[9]
$ZnFe_2O_4$	138.95 at 2 mV s^{-1}	–	–	>90% after 1000 cycles	[9]
$CoFe_2O_4$	65.5 at 10 mV s^{-1}	–	–	90.9% after 1000 cycles	[13]
rGO-$CoFe_2O_4$	112.9 at 10 mV s^{-1}	–	–	91.3% after 1000 cycles	[13]
$CoFe_2O_4$	142 at 2 mV s^{-1}	–	–	71.8% after 1000 cycles	[14]
$NiFe_2O_4$	50 at 0.5 A g^{-1}	–	–	78.6% after 2000 cycles	[15]
rGO/$NiFe_2O_4$	215.7 at 0.5 A g^{-1}	–	–	89.4% after 2000 cycles	[15]
$ZnFe_2O_4$	131 at 0.1 A g^{-1}	–	–	92% after 1000 cycles	[17]
rGO-$CoFe_2O_4$	123.2 F/cm^2 at 5 mA cm^{-2}	–	–	78.1% after 1000 cycles	[19]
$CuCoFe_2O_4$	221 at 5 mV s^{-1}	7.90	1711.95	80% after 200 cycles	[20]
$ZnFe_2O_4$ NPs	94 at 0.5 A g^{-1}	–	–	32% after 5000 cycles	[21]
$ZnFe_2O_4$/NRG	244 at 0.5 A g^{-1}	–	–	83.8% after 5000 cycles	[21]
$ZnFe_2O_4$/*g*-C_3N_4	103 at 10 A g^{-1}	–	–	94% after 500 cycles	[22]
$ZnFe_2O_4$/GCE	175 at 5 A g^{-1}	–	–	82.75% after 1000 cycles	[23]
$Co_{0.5}Ni_{0.5}Fe_2O_4$	113 at 5 mV s^{-1}	–	–	120% after 1000 cycles	[25]
$Ni_{0.6}Zn_{0.4}Fe_2O_4$	186.61 at 1 A g^{-1}	5.24	224.65	–	[26]
$Ni_{0.8}Zn_{0.2}Fe_2O_4$	136.55 at 1 A g^{-1}	3.84	101.32	–	[26]
Activated carbon 850	138.12 at 5 mV s^{-1}	9.6	87.86	–	[42]
Activated carbon	153.66 at 1 A g^{-1}	9.27	329.44	86.9 after 10000 cycles	[43]
AC-TiO_2	147.02 at 2 mV s^{-1}	8.02	1186.51	105% after 1000 cycles	[44]
$Ni_{0.5}Zn_{0.5}Fe_2O_4$	250 at 1 A g^{-1}	22.31	400	91.54% after 200 cycles	This work

Arts College (Autonomous), Chennai, for their support in completing this work. Dr. S. Paramagururaj, Department of English, Government Arts College (Autonomous), Chennai, for assistance in language editing of the manuscript. The authors also express their gratitude to the Government College of Engineering, Bargur and PSG Institute of Advanced studies, Coimbatore and Dr. M. Victor Antony Raj, Department of Physics, Loyola College (Autonomous), Chennai, for providing the instrumental characterisation facilities and Dr. Harini Saravana Muthu, Nano R & D, Research Associate, Kothari Sugars and Chemicals Ltd. for supporting the electrochemical instruments. Finally, P. Balaraman (M.Sc. Physics, Govt. Arts College, Chennai) and Dr. A. Shanmugavani (Asst. Prof., Department of Physics, Sri G.V.G. Vishalakshi College for Women, Udumalpet) for their support in data interpretation, manuscript preparation and completion of this work.

CONFLICT OF INTEREST

The authors declare that there is no conflict of interests regarding the publication of this article.

DECLARATION OF AI-ASSISTED TECHNOLOGIES

During the preparation of this manuscript, the authors used an AI-assisted tool(s) to improve the language. The authors reviewed and edited the content and take full responsibility for the published work.

REFERENCES

1. A. Shuja, H.R. Khan, I. Murtaza, S. Ashraf, Y. Abid, F. Farid and F. Sajid, *J. Alloys Compd.*, **1009**, 176924 (2024); https://doi.org/10.1016/j.jallcom.2024.176924
2. A. Afreen, M.B.B. Hamida, M.N. Hussain, M. Javaid, N. Alrasheedi, J. Iqbal, A. Haider and S.M. Shah, *Mater. Adv.*, (2026); https://doi.org/10.1039/D5MA01229E
3. A.G. Olabi, Q. Abbas, A. Al Makky and M.A. Abdelkareem, *Energy*, **248**, 123617 (2022); https://doi.org/10.1016/j.energy.2022.123617
4. P. Simon and Y. Gogotsi, *Nat. Mater.*, **7**, 845 (2008); https://doi.org/10.1038/nmat2297
5. G. Wang, L. Zhang and J. Zhang, *Chem. Soc. Rev.*, **41**, 797 (2012); https://doi.org/10.1039/c1cs15060j
6. D. P. Dubal, O. Ayyad, V. Ruiz and P. Gomwz-Romero, *Chem. Soc. Rev.*, **44**, 1777 (2015); https://doi.org/10.1039/C4CS00266K
7. S.S. Shah and M.A. Aziz, *J. Chem. Environ.*, **3**, **1** (2024); https://doi.org/10.56946/jce.v3i1.309
8. S.A. Delbari, L.S. Ghadimi, R. Hadi, S. Farhoudian, M. Nedaei, A. Babapoor, A.S. Namini, Q.V. Le, M. Shokouhimehr, M.S. Asl and M. Mohammadi, *J. Alloys Compd.*, **857**, 158281 (2021); https://doi.org/10.1016/j.jallcom.2020.158281
9. M.L. Aparna, A.N. Grace, P. Sathyanarayanan and N.K. Sahu, *J. Alloys Compd.*, **745**, 385 (2018); https://doi.org/10.1016/j.jallcom.2018.02.127
10. S.J. Salih and W.M. Mahmood, *Heliyon*, **9**, e16601 (2023); https://doi.org/10.1016/j.heliyon.2023.e16601
11. D. Ham, J. Chang, S.H. Pathan, W.Y. Kim, R.S. Mane, B.N. Pawar, O.S. Joo, H. Chung, M.Y. Yoon and S.H. Han, *Curr. Appl. Phys.*, **9S1**, S98 (2009); https://doi.org/10.1016/j.cap.2008.08.042
12. H. Palani, T. Gopalakrishnan and A. Rastogi, *AIP Conf. Proc*, **2995**, 020190 (2024); https://doi.org/10.1063/5.0178237
13. I. Kotutha, T. Duangchuen, E. Swatsitang, W. Meewasana, J. Khajonrit and S. Maensiri, *Ionics*, **25**, 5401 (2019); https://doi.org/10.1007/s11581-019-03114-1
14. L. Lv, Q. Xu, R. Ding, L. Qi and H. Wang, *Mater. Lett.*, **111**, 35 (2013); https://doi.org/10.1016/j.matlet.2013.08.055
15. Y.Z. Cai, W.Q. Cao, P. He, Y.L. Zhang, and M.S. Cao, *Mater. Res. Express*, **6**, 105535 (2019); https://doi.org/10.1088/2053-1591/ab3fff
16. M. Bohra, V. Alman and R. Arras, *Nanomaterials*, **11**, 1289 (2021); https://doi.org/10.3390/nano11051286

17. M. Zhu, X. Zhang, Y. Zhou, C. Zhuo, J. Huang and S. Li, *RSC Adv.*, **5**, 39270 (2015); https://doi.org/10.1039/c5ra00447k
18. K. Sathiyamurthy, C. Rajeevgandhi, S. Bharanidharan, P. Sugumar and S. Subashchandrabose, *Chem. Data Collect.*, **28**, 100477 (2020); https://doi.org/10.1016/j.cdc.2020.100477
19. P. He, K. Yang, W. Wang, F. Dong, L. Du and Y. Deng, *Russ. J. Electrochem.*, **49**, 359 (2013); https://doi.org/10.1134/S1023193513040101
20. B. Bhujun, M.T.T. Tan and A.S. Shanmugam, *Results Phys.*, **7**, 345 (2017); https://doi.org/10.1016/j.rinp.2016.04.010
21. L. Li, H. Bi, S. Gai, F. He, P. Gao, Y. Dai, X. Zhang, D. Yang, M. Zhang and P. Yang, *Sci. Rep.*, **7**, 43116 (2017); https://doi.org/10.1038/srep43116
22. B. Palanivel, S.D.M. Perumal, T. Maiyalagan, V. Jayarman, C. Ayyappan and M. Alagiri, *Appl. Surf. Sci.*, **498**, 143807 (2019); https://doi.org/10.1016/j.apsusc.2019.143807
23. M. Saraf, K. Natarajan, A.K. Gupta, P. Kumar, R. Rajak and S.M. Mobin, *Mater. Res. Express*, **6**, 095534 (2018); https://doi.org/10.1088/2053-1591/ab3339
24. K. Sathiyamurthy, C. Rajeevgandhi, L. Guganathan, S. Bharanidharan and S. Savithiri, *J. Mater. Sci. Mater. Electron.*, **32**, 11593 (2021); https://doi.org/10.1007/s10854-021-05764-2
25. Y. Lin, J. Wang, H. Yang, L. Wang and M. Cao, *Mater. Sci. Eng. B*, **228**, 103 (2018); https://doi.org/10.1016/j.mseb.2017.11.013
26. S.O. Costa and V.M.S. Verenkar, *Mater. Res. Bull.*, **176**, 112778 (2024); https://doi.org/10.1016/j.materresbull.2024.112778
27. A. Sutka and G. Mezinskis, *Front. Mater. Sci.*, **6**, 128 (2012); https://doi.org/10.1007/s11706-012-0167-3
28. H. Dubey, C. Verma, U. Rai, A. Kumar and P. Lahiri, *Indian J. Chem.*, **58A**, 454 (2019).
29. A. Rayar and G.D. Prasanna, *IOP Conf. Ser. Mater. Sci. Eng.*, **1300**, 012046 (2024); https://doi.org/10.1088/1757-899x/1300/1/012046
30. S. Gawali, P.S. Patil, Y.P. Ubale, V. Surashe and K.M. Jadhav, *Asian J. Chem.*, **37**, 2031 (2025); https://doi.org/10.14233/ajchem.2025.34062
31. V.D. Patil, D.A. Patil, A.L. Jadhav, S.L. Jadhav, A.V. Kadam and S.R. Dandwate, *Discov. Electrochem.*, **1**, 2 (2024); https://doi.org/10.1007/s44373-024-00003-9
32. D. Briggs, in eds.: D.E. Packham, X-ray photoelectron Spectroscopy (XPS), Handbook of Adhesion, John Wiley & Sons, Ltd., edn. 2, Chap. 22, p. 621 (2005).
33. M.M. El-Masry and M.M. Arman, *Sci. Rep.*, **15**, 16636 (2025); https://doi.org/10.1038/s41598-025-99604-6
34. E. Samuel, A. Aldalbahi, M. El-Newehy, H. El-Hamshary and S.S. Yoon, *J. Alloys Compd.*, **852**, 156929 (2021); https://doi.org/10.1016/j.jallcom.2020.156929
35. Q. Yu, Y. Su, R. Tursun and J. Zhang, *RSC Adv.*, **9**, 13173 (2019); https://doi.org/10.1039/c9ra01076a
36. A. Bajorek, C. Berger, M. Dulski, P. Lopadczak, M. Zubko, K. Prusik, M. Wojtyniak, A. Chrobak, F. Grasset and N. Randrianantoandro, *J. Phys. Chem. Solids*, **129**, 1 (2019); https://doi.org/10.1016/j.jpcs.2018.12.045
37. X. Gao, W. Wang, J. Bi, Y. Chen, X. Hao, X. Sun and J. Zhang, *Electrochim. Acta*, **296**, 181 (2019); https://doi.org/10.1016/j.electacta.2018.11.054
38. B. Albini, S. Restelli, M. Ambrosetti, M. Bini, F. D'Amico, M.C. Mozzati and P. Galinetto, *J. Mater. Sci. Mater. Electron.*, **34**, 1030 (2023); https://doi.org/10.1007/s10854-023-10464-0
39. A.V. Shinde, S.J. Patil, S. Hwang, G.S.R. Raju, Y. Huh, Y. Han and N.R. Chodankar, *Ceram. Int.*, **47**, 16333 (2021); https://doi.org/10.1016/j.ceramint.2021.02.213
40. X. Guo, C. Yang, G. Huang, Q. Mou, H. Zhang and B. He, *J. Alloys Compd.*, **764**, 128 (2018); https://doi.org/10.1016/j.jallcom.2018.06.054
41. S. Suresh and V. Sindhu, *Ionics*, **29**, 843 (2023); https://doi.org/10.1007/s11581-022-04846-3
42. A. Ahmad, M.A. Gondal, M. Hassan, R. Iqbal, S. Ullah, A.S. Alzahrani, W.A. Memon, F. Mabood and S. Melhi, *ACS Omega*, **8**, 21653 (2023); https://doi.org/10.1021/acsomega.3c01065
43. C.Y. Wu, C.Y. Chang, S.W. Tsai, S.C. Lin, T.C. Hsu and T.H. Hsieh, *ACS Appl. Energy Mater.*, **7**, 6873 (2024); https://doi.org/10.1021/acsaem.4c00732
44. T.M.W.J. Bandara, A.M.B.S. Alahakoon, B.E. Mellander and I. Albinsson, *Carbon Trends*, **15**, 100359 (2024); https://doi.org/10.1016/j.cartre.2024.100359